CeO_2 and Co_3O_4–CeO_2 nanoparticles: effect of the synthesis method on the structure and catalytic properties in COPrOx and methanation reactions

Leonardo F. Peiretti, Nuria Navascués, Inés S. Tiscornia & Eduardo E. Miró

Journal of Materials Science
Full Set - Includes `Journal of Materials Science Letters'

ISSN 0022-2461
Volume 51
Number 8

J Mater Sci (2016) 51:3989-4001
DOI 10.1007/s10853-015-9717-2

Springer

J Mater Sci (2016) 51:3989–4001
DOI 10.1007/s10853-015-9717-2

CeO_2 and Co_3O_4–CeO_2 nanoparticles: effect of the synthesis method on the structure and catalytic properties in COPrOx and methanation reactions

Leonardo F. Peiretti[1] · Nuria Navascués[2] · Inés S. Tiscornia[1] · Eduardo E. Miró[1]

Received: 29 September 2015 / Accepted: 30 December 2015 / Published online: 12 January 2016

Abstract CeO_2 and Co_3O_4–CeO_2 nanoparticles were synthesized, thoroughly characterized, and evaluated in the COPrOx reaction. The CeO_2 nanoparticles were synthesized by the diffusion-controlled precipitation method with ethylene glycol. A notably higher yield was obtained when H_2O_2 was used in the synthesis procedure. For comparison, two commercial samples of CeO_2 nanoparticles (Nyacol®)—one calcined and the other sintered—were also studied. Catalytic results of bare CeO_2 calcined at 500 °C showed a strong influence of the method of synthesis. Despite having similar BET area values, the CeO_2 synthesized without H_2O_2 was the most active sample. Co_3O_4–CeO_2 catalysts with three different Co/(Co + Ce) atomic ratios, 0.1, 0.3, and 0.5, were prepared by the wet impregnation of the CeO_2 nanoparticles. TEM and STEM observations showed that impregnation produced mixed oxides composed of small CeO_2 nanoparticles located both over the surface and inside the Co_3O_4 crystals. The mixed oxide catalysts prepared with a cobalt atomic ratio of 0.5 showed methane formation, which started at 200 °C due to the reaction between CO_2 and H_2. However, above 250 °C, the reaction between CO and H_2 became important, thus contributing to CO elimination with a small H_2 loss. As a result, CO could be totally eliminated in a wide temperature range, from 200 to 400 °C. The methanation reaction was favored by the reduction of the cobalt oxide, as suggested by the TPR experiments. This result is probably originated in Ce–Co interactions, related to the method of synthesis and the surface area of the mixed oxides obtained.

Introduction

The field of nanoscience has become the focus of considerable research efforts due to its new and recently discovered applications [1, 2]. Nanocatalysts are continuously under development for hydrogen production, purification, and storage. When hydrogen is obtained through hydrocarbon steam reforming, a purification stage must be included before the gas mixture reaches the proton exchange membrane (PEM). CO Preferential Oxidation (COPrOx) is one of the most promissory methods to decrease concentrations of CO up to 10 ppm—or less— at small scale [3]. Although the oxidation of CO is the most widely studied method, methanation is also analyzed as an alternative reaction [4–6]. A wide variety of catalysts with Pt, CeO_2, CuO_x, CoO_x, and nanosized Au are under study for COPrOx [3]. CeO_2 is also extensively studied due to its high oxygen storage capacity (OSC) which is closely

Electronic supplementary material The online version of this article (doi:10.1007/s10853-015-9717-2) contains supplementary material, which is available to authorized users.

✉ Inés S. Tiscornia
itiscornia@fiq.unl.edu.ar

Leonardo F. Peiretti
lfpeiretti@fiq.unl.edu.ar

Nuria Navascués
nurian@unizar.es

Eduardo E. Miró
emiro@fiq.unl.edu.ar

[1] Instituto de Investigaciones en Catálisis y Petroquímica, INCAPE (FIQ, UNL-CONICET), Santiago del Estero 2829, S3000AOM Santa Fe, Argentina

[2] Department of Chemical Engineering, Nanoscience Institute of Aragon (INA), 50018 Saragossa, Spain

linked to the ease with which cerium can change between its oxidation states [7].

In a previous work, we studied several methods of synthesis in order to obtain active CeO_2 nanoparticles for the COPrOx reaction [8]. We showed that the thermal decomposition of precursors and solvents after the synthesis by the controlled precipitation method is a complex process that gives place to the formation of several species adsorbed on the surface of the materials. Organic species such as di-σ/π-acetylene and di-σ/π-vinylidene remain on the surface of some of the samples at temperatures near 500 °C together with different types of carbonates and nitrates, indicating that at least this temperature is necessary to obtain non-contaminated ceria nanoparticles.

We also studied the COPrOx reaction over a Co/CeO_2 catalyst washcoated on a cordierite monolith, but no attempt was made to study different synthesis routes for obtaining mixed oxide catalysts under the form of nanoparticles [9].

In a recent work, Gómez-Cuaspud et al. [10] investigated the synthesis of nanosized Co_3O_4, NiO, and CuO oxides by the polymerization–combustion method and evaluated them in the selective oxidation of CO. They reported that the activity of Co_3O_4 is 3 times higher than that of NiO and CuO. They showed that for the Co_3O_4 the temperature increase favors the CO conversion, resulting in complete conversion at 200 °C. However, for higher temperatures the hydrogen oxidation becomes preferential, and the CO conversion decreases. In their work, the formation of methane through the methanation of CO and CO_2 is also suggested, but methane is further oxidized to CO_2 and/or converted in CO due to reforming reactions.

Woods et al. [11] synthesized CoO_x/CeO_2 catalysts with high surface area (78 m^2/g) and tested them in the preferential oxidation of CO. They observed three distinct temperature regions of catalyst activity corresponding to CO oxidation, H_2 oxidation, and methanation. Below 175 °C, CO oxidation was dominant; between 175 and 275 °C, it competed with H_2 combustion and above 275 °C, methanation was the main reaction. Additionally, they studied a wide range of conditions as WHSV, and O_2 and H_2 concentration.

Taking into account the above-mentioned studies, the aim of this work is to present how the different synthesis methods can affect the activity in the COPrOx for the bare CeO_2, and also to show how the impregnation with cobalt produces a new kind of nanoparticle with a higher activity. Our Co_3O_4–CeO_2 catalyst can eliminate CO in a wide temperature range due to the occurrence of both COPrOx and methanation reactions. The synthesized solids were thoroughly characterized by XRD, BET, TPR, FTIR, TEM, and XPS.

Experimental

Materials

Cerium nitrate [$Ce(NO_3)_3 \cdot 6H_2O$, 99 %] and cobalt nitrate [$Co(NO_3)_2 \cdot 6H_2O$, 98 %] from Sigma-Aldrich® were the solid precursors used for the synthesis. Hydrogen peroxide (30 %) from Anedra® and aqueous ammonia solution (28–30 %), ethylene glycol (EG ≥99.5 %), and ethanol (99.5 %) from Cicarelli® were used without further purification. A solution of EG/H_2O 70 %V was prepared to dissolve the precursors and obtain the 0.2 M precursor solutions. The precipitant (NH_4OH) aqueous solution concentration was ca. 3 M. The commercial suspension of CeO_2 nanoparticles stabilized with acetate as counter ions were obtained from Nyacol®.

Synthesis methods

CeO_2 nanoparticles

CeO_2 nanoparticles were synthesized by the diffusion-controlled precipitation method with and without H_2O_2. The procedure without peroxide was reported in our previous work [8]. In this method, the solution of 0.2 M of $Ce(NO_3)_3$ dissolved in EG/H_2O (70 %V) was added with a syringe pump to the ca. 3 M NH_4OH solution. A slight optimization was made by lowering the flow of the syringe pump to 1.5 mL/min for the samples synthesized in this work. The suspension obtained was aged under stirring for 24 h. Three centrifugations at 12,000 rpm (14,810 RCF), with intermediate washes with ethanol and water, were performed to clean the precipitated nanoparticles. The other procedure of synthesis, with peroxide, was an improvement of the method described, which allowed a higher nanoparticle yield. The variation was that a stoichiometric amount of H_2O_2 ($Ce^{3+}/H_2O_2 = 2{:}1$) was added to the $Ce(NO_3)_3$ solution in EG/H_2O (70 %V), and left to react for 10 min before adding it to the NH_4OH solution. Thereafter, the suspension was aged for 10 min. Both samples, with and without H_2O_2, were dried at 70 °C overnight. On the other hand, CeO_2 commercial powder was obtained by evaporation of the Nyacol® acetic acid suspension at 130 °C overnight. All the samples were calcined under air flow (100 mL/min) at 500 °C for 3 h with a heating ramp of 2 °C/min. A determined amount of the dried commercial sample was sintered at 800 °C, in the same way as calcination, in order to obtain a specific surface area remarkably lower compared with the other samples.

The samples were denominated 4EG-Ce500 for the previously reported method [8], OxEG-Ce500 for the

improved method with H_2O_2, and Ny500 and NySint, for the commercial samples calcined at 500 °C and sintered, respectively.

In order to compare the effectivity of the different synthesis methods, we defined the yield of CeO_2 nanoparticles as

$$\eta_{CeO_2} = \frac{m_{CeO_2,c}}{m_{CeO_2,teo}} \times 100\,\%$$

where $m_{CeO_2,c}$ is the mass of the CeO_2 after calcination and $m_{CeO_2,teo}$ is the mass of CeO_2 assuming that all $Ce(NO_3)_3$-$6H_2O$ was converted.

Co_3O_4–CeO_2 nanoparticles

Cobalt was added to the CeO_2 particles by wet impregnation. 200 mg of ceria (4EG-Ce500, OxEG-Ce500, Ny500 and NySint) were impregnated with 150 μL of a $Co(NO_3)_2$ aqueous solution with the adequate concentration to obtain a [Co/(Co + Ce)] molar ratio = 0.5. OxEG-Ce500 and Ny500 were also impregnated to obtain 0.3 and 0.1 Co molar ratios. The solution was added in aliquots to the solid and mixed manually until a paste was formed. The product was dried at 130 °C and calcined at 500 °C with the same procedure as that performed with CeO_2. This method allows obtaining an amount of Co close to the theoretical one.

Characterization

Structural and textural properties

XRD measurements were performed at room temperature with a Rigaku® diffractometer, D/max 2500 model, equipped with a rotating Cu anode ($\lambda = 0.154056$ nm) working at 40 kV and 80 mA, and a graphite monochromator to select the Cu $K_{\alpha 1,2}$. The measurement conditions were 2θ angle between 15° and 90°, step = 0.03°, and $t = 1$ s/step. The crystallite size was estimated by the Scherrer equation. The Scherrer constant adopted was 0.9 and the FWHM was corrected using an Si standard measured in the same equipment.

Specific surface areas were obtained with a TRISTAR 3000 surface area and porosity measurement instrument from Micromeritics®. Samples were previously evacuated at 200 °C for 8 h under vacuum. Adsorption isotherms were determined by N_2 adsorption over the samples at 77 K. Surface areas and pore diameters were calculated by applying the Brunauer–Emmett–Teller (BET) and the Barrett–Joyner–Halenda (BJH) equations to the adsorption isotherms, respectively.

The TEM analysis was performed on an FEI® transmission electron microscope, Tecnai T20 model with an electron source of 200 kV. Images of the solids were taken by suspending them in isopropanol. For the STEM analysis, we used an FEI® transmission electron microscope, Tecnai F30 model with an electron source of 300 kV, equipped with a XEDS system with an Li-drifted Si detector, and an energy resolution of 130 eV.

Chemical species

Fourier transform infrared spectroscopy (FTIR) was carried out using a Shimadzu® FTIR spectrometer, IRPrestige-21 model. All samples were weighed and diluted in a known amount of KBr in order to relatively quantify the functional groups present.

The Temperature Programed Reduction (TPR) analyses were performed on a Micromeritics® analyzer, AutoChem 2950 HP model. 50 mg of catalyst was weighed and placed on a U-tube reactor. A 5 % H_2/Ar gas mixture was used to perform the analysis between room temperature and 900 °C, with a heating ramp of 5 °C/min and a gas flow of 80 mL/min. The pretreatment consisted in drying with Ar at 200 °C (10 °C/min) during 30 min. The catalysts used in the reaction were also oxidized prior to the drying step with a 21 % O_2/Ar gas mixture under the same conditions used during calcination. The CeO_2 and Co_3O_4 standards were produced by calcining the nitrate precursors at 600 °C with a heating ramp of 2 °C/min.

The surface features of the catalysts were studied in a multi-technique system (SPECS) equipped with a dual Mg/Al X-ray source and a hemispherical PHOIBOS 150 analyzer operating in the fixed analyzer transmission (FAT) mode. The spectra were obtained with a pass energy of 30 eV and with an Mg Kα X-ray source operated at 200 W and 12 kV. The working pressure in the analyzing chamber was $<5 \times 10^{-10}$ kPa. The spectral regions corresponding to Ce 3d, Co 2p, and O 1s core levels were recorded for each sample. The static charge of the samples was corrected by referencing all binding energies (BEs) to the C 1s peak (BE = 284.6 eV). The data treatment was performed with the Casa XPS program (Casa Software Ltd., UK). The areas of the peaks were computed by fitting the experimental spectra to the Gaussian/Lorentzian product formula where the mixing was 30 % of a Lorentzian curve. The background used for C 1s, O 1s, and Co 2p species was Shirley type, and linear for Ce 3d. Surface atom ratios were calculated from peak area ratios adjusted by atomic relative sensitivity factors (RSFs), transmission and escape depth (mean free path). Regions of Ce 3d and O 1s were fitted according to Konysheva et al. [12] and Fang et al. [13], respectively.

Catalytic tests

Preferential CO oxidation experiments were performed in a fixed-bed flow reactor. The reaction mixture consisted of

CO 1 %, O_2 1 %, H_2 40 %, and He balance. The weight/total flow ratio was adjusted to 2.1 mg/cm^3 min by means of mass flow controllers. The CO conversion (x_{CO}), CH_4 production (P_{CH4}), and the selectivity towards CO_2 (S_{CO2}) were defined as

$$x_{CO} = \frac{[CO]^0 - [CO]}{[CO]^0} \times 100\,\%$$

$$P_{CH_4} = \frac{[CH_4]}{[CO]^0} \times 100\,\%$$

$$S_{CO_2} = \frac{[CO]^0 - [CO] - [CH_4]}{2\left([O_2]^0 - [O_2]\right)} \times 100\,\%,$$

where [CO], [CH_4], and [O_2] are reactor exit concentrations and $[CO]^0$ and $[O_2]^0$ represent feed concentrations, which were measured with a chromatograph GC-2014 Shimadzu® equipped with a TCD cell (sensitivity: 40,000 mV × mL/mg).

Results and discussion

CeO_2 nanoparticles: characterization and catalytic properties

The diffusion-controlled precipitation methods of synthesis employed in this work resulted in different nanoparticle yields (defined in "CeO_2 nanoparticles" section). The addition of H_2O_2 notoriously increased the yield from 28.9 to 96.2 %.

Figure 1 shows the XRD results obtained for the samples studied. It can be seen that patterns corresponding to the CeO_2 fluorite structure were observed in all samples (Fig. 1a). In Fig. 1b, a shift to lower 2θ angles can be observed in the pattern of the samples calcined at 500 °C. This could indicate the presence of structural strains (higher lattice constant) not observed in the sintered sample [14, 15]. On the other hand, the greater peak intensities for OxEG-Ce500 and NySint could be due to a higher crystallinity, produced for H_2O_2 oxidation or calcination temperature, respectively.

The structural and textural properties of the samples are summarized in Table 1. Crystallite size and BET surface area were similar for all samples, except for NySint. This is directly related to the higher temperature used in its thermal treatment. It is interesting to note that all the samples were practically nonporous, since pore size was of the same order of magnitude as particle size, which is characteristic of the voids formed between nanoparticles (the pore size distribution with BJH analysis can be found in the supplementary information: 3.1.1).

The TEM Images show irregular particles with sharpened borders (Fig. 2). Some extent of agglomeration is visible and predictable due to drying and calcination treatments. Crystal planes are observed in some particles, in agreement with XRD measurements (insets in Fig. 2). Measured TEM particle sizes follow almost the same trend as crystallite size (Table 1).

Figure 3 shows the infrared spectra of the CeO_2 samples, which were performed quantitatively to observe the relative amount of carbonate and peroxide species, since it could be important in the prediction of their redox activity. It is shown that, although the concentration differences of carbonate species were small, 4EG-Ce500 showed the least amount. On the other hand, the higher carbonate concentration for OxEG-Ce500 could be attributed to the products from the EG oxidation by the H_2O_2 [16]. Additionally,

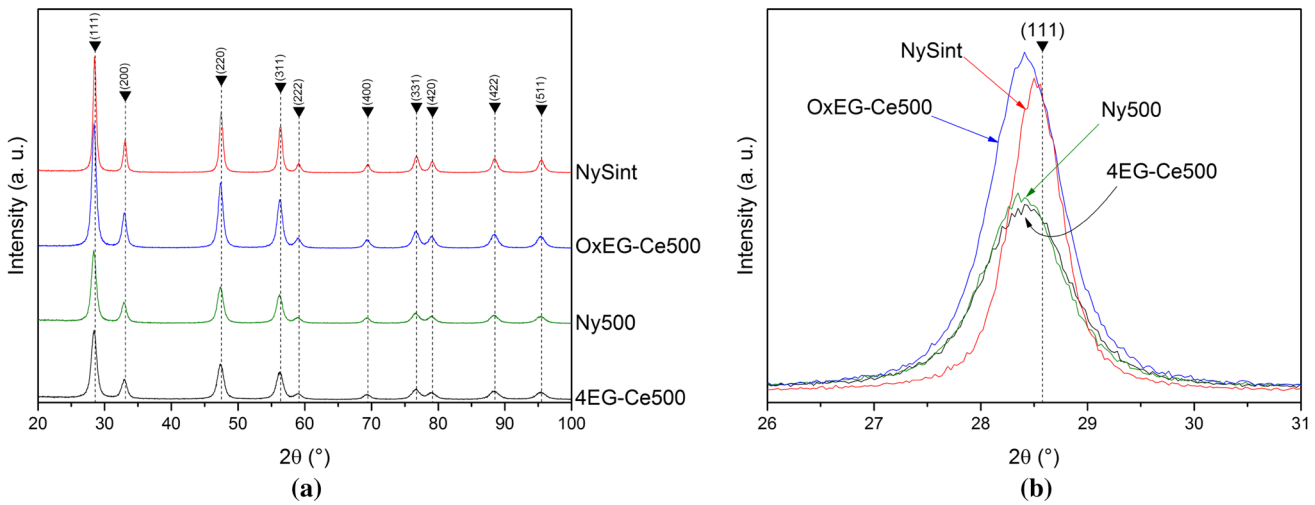

Fig. 1 XRD measurements of the CeO_2 samples. **a** From $2\theta = 20°–100°$ and **b** shift observed (detailed figure)

Table 1 Structural and textural properties of ceria nanoparticles

Sample	Crystallite size (nm)	BET (m^2/g)	Pore diameter BJH (nm)	Particle size[a] (nm)
4EG-Ce500	9.1 ± 1.1	67.7	2.5	6.6 ± 2.1
OxEG-Ce500	12.0 ± 0.8	62.2	2.7	8.0 ± 2.6
Ny500	10.1 ± 1.3	56.4	2.4	8.7 ± 3.0
NySint	18.0 ± 2.4	6.7	2.9	17.3 ± 7.8

[a] Determined by TEM

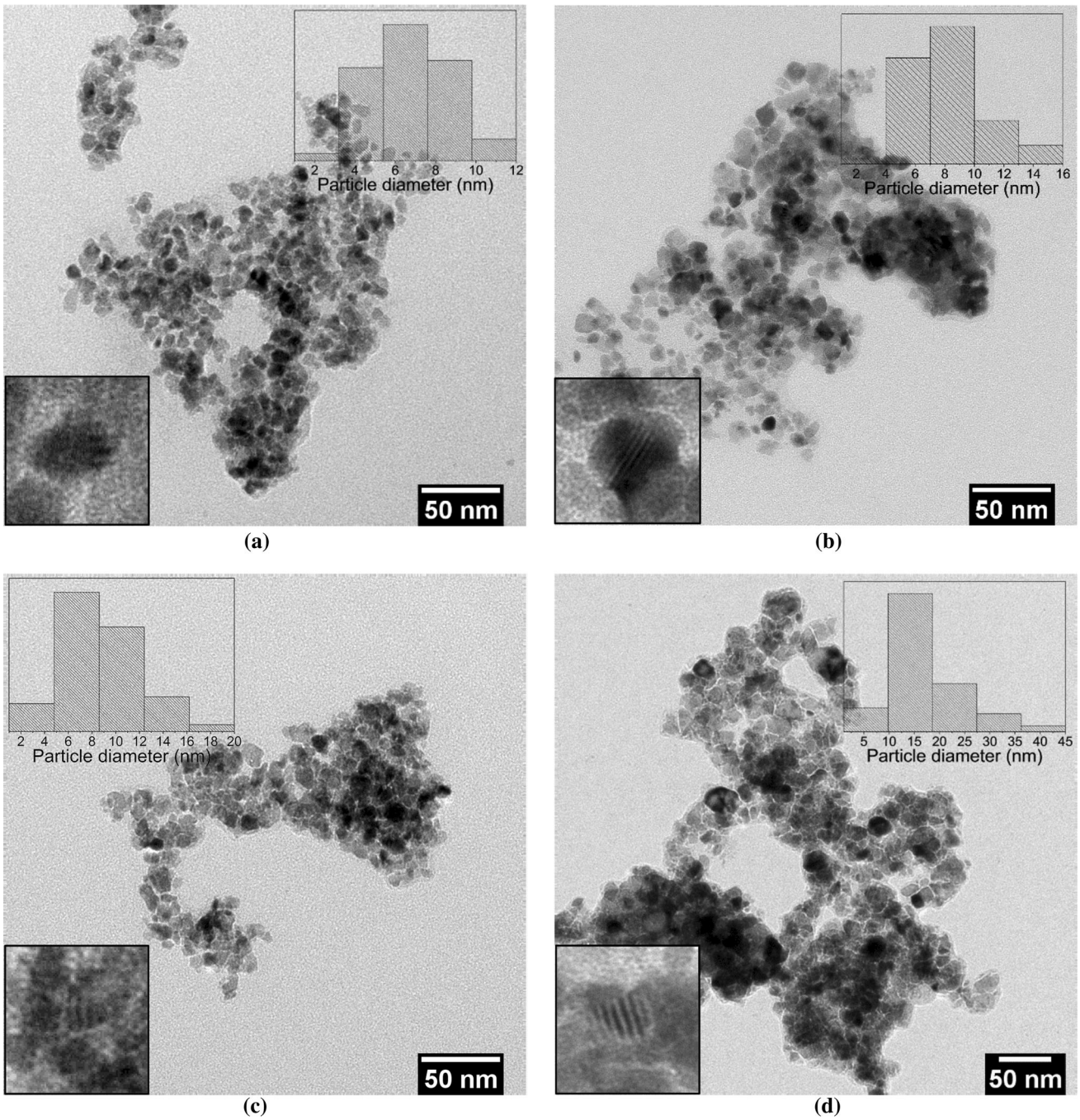

Fig. 2 TEM images of the synthesized samples. **a** 4EG-Ce500, **b** OxEG-Ce500, **c** Ny500, and **d** NySint

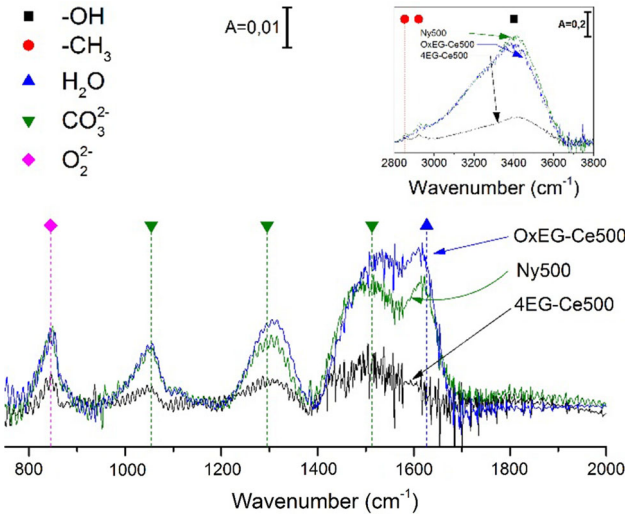

Fig. 3 FTIR for fresh CeO_2 samples

some methyl groups could be observed in all samples as rests of organic molecules (EG and acetic acid for the commercial sample). A higher temperature could be used to eliminate them [17], but the area decrease and previous results [8] led to the calcination temperature selected (500 °C).

Conversion of CO and selectivity towards CO_2 are shown in Fig. 4 for the CeO_2 samples. The most active sample was 4EG-Ce500, whereas NySint presented the lowest CO conversion. The behavior of the sintered sample could be explained due to the decrease of the available BET surface area. Furthermore, the CO conversion values of the NySint sample divided by its BET surface area were similar to those of Ny500 (divided by its own area), indicating that the lower conversion of CO was almost exclusively due to the decrease of the BET surface area (Fig. 5).

The temperatures when the CO conversion was 50 % (T_{50}) were 184, 267, and 308 °C for 4EG-Ce500, Ny500, and OxEG-Ce500, respectively. This fact could be attributed to the synthesis method. For OxEG-Ce500 and Ny500 samples, the higher amounts of carbonate species observed by FTIR after calcination (Fig. 3) could be blocking more active sites than in 4EG-Ce500, lowering their oxidative capacity. In fact, both solids presented similar amounts of carbonates and profiles of the CO conversion curves.

In order to analyze the species present on the surface of the CeO_2 samples, an XPS study was performed. The fitting of the spectra is summarized in Table 2, and the BEs obtained are presented in the supplementary information (Table S1). Superficial defects, given by the Ce^{+3}/Ce ratio and the oxide stoichiometry (δ), were similar in all the samples. For similar BET surface areas, the CeO_2 that exhibited the lowest temperature at the 50 % CO conversion presented the highest surface O/Ce ratio (4EG-Ce500). Furthermore, this sample also showed the highest values for the O_{II} and O_{III} regions. The former includes the species adsorbed on O^{2-} vacancies—carbonates, hydroxiles, peroxides, and superoxides—whereas the latter includes the organic oxygen, molecular H_2O, nitrites, and nitrates [12, 13, 18–21]. According to Stoch et al. [22], the O_{II}/O–C=O ratio near 3 means carbonate contamination; however, this correlation was smaller for all samples (Table 2). Therefore, the carbonates present on the surface were non-stoichiometric, and presented the same trend observed by FTIR (Fig. 3). Sample NySint cannot be compared due to the high BET area difference.

The TPR study of the CeO_2 samples supported the XPS information showing that the highest CO conversion is related to the lower reduction temperature and the higher H_2 consumption (Table 3). TPR profiles of the CeO_2

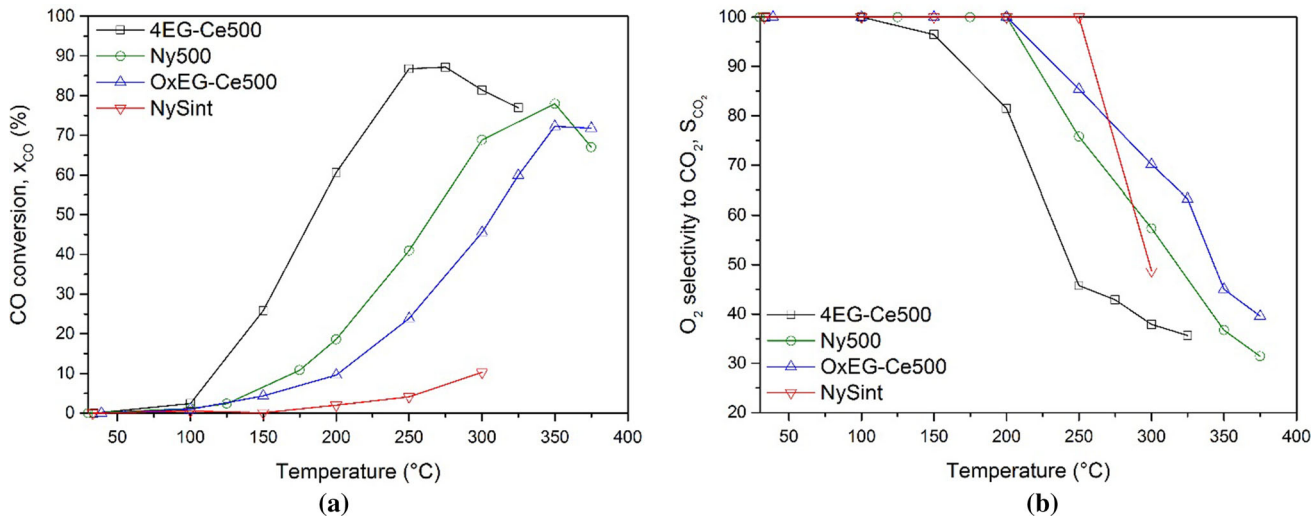

Fig. 4 Catalytic performance on COPrOx for CeO_2 nanoparticles. **a** CO conversion and **b** selectivity of O_2 to CO_2

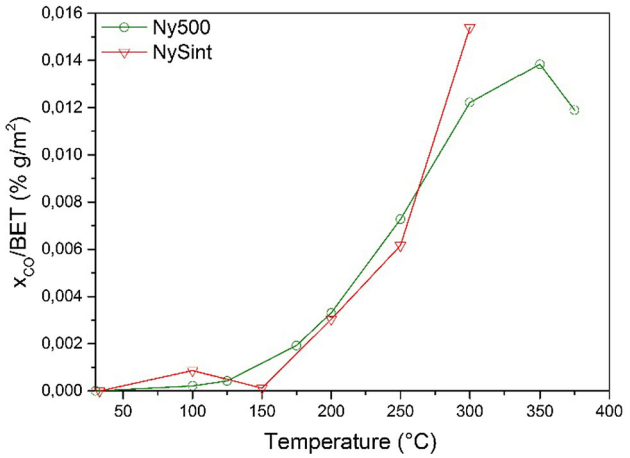

Fig. 5 CO conversion per unit area (BET) for commercial samples: calcined at 500 °C (Ny500) or sintered (NySint)

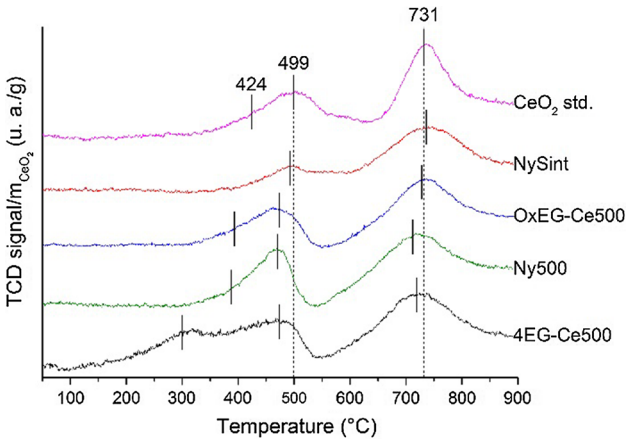

Fig. 6 TPR profiles of CeO_2 samples and the standard

nanoparticles showed lower reduction temperatures than the standard for the first and second peaks (Fig. 6). These signals are attributed to the successive reduction steps of the superficial oxygen of CeO_2 [23–26], in agreement with the reduction easiness of the nanoparticles of this oxide due to their higher crystalline stress [17] (Fig. 1). It is interesting to note that the reduction peaks of the NySint sample showed temperature values similar to those of the standard.

In brief, we found that oxygen vacancies (Ce^{+3} measured by XPS) were not important to explain the activity difference, since the δ values (Table 2) were similar for all the samples. However, the O quantified by XPS was key in the catalytic behavior of the CeO_2 samples. XPS measurements require ultra-high vacuum (UHV) and the higher relation O/Ce could mean a higher amount of O_2 strongly adsorbed. Nevertheless, some other species could be blocking the defects (Ce^{+3} or δ) and lowering the O_2 adsorbed. We have shown that the amount of carbonates that block the adsorption sites for O_2 is higher for the less active sample (Table 2; Fig. 3). Therefore, in our case, the amount of defects seemed to be similar, but the presence of the adsorbed carbonates—which do not contribute to the conversion of CO—lowered the CeO_2 activity. The lower reduction temperatures for the most active sample (4EG-Ce500) in the TPR (Table 3; Fig. 6) supported the existence of this higher amount of O_2 adsorbed, which is also more accessible due to the lower CO_2 concentration.

Regarding the O_2 selectivity to CO_2 for the CeO_2 samples, it decreased monotonically with the temperature rise (Fig. 4b). This result shows that the conversion of CO into CO_2 is accompanied by the oxidation of H_2 into H_2O. This fact, widely reported, made it necessary to include

Table 2 XPS study of superficial species and catalytic performance

Sample	O_{II}/O–C=O	O/Ce	O_{II}/Ce	O_{III}/Ce	Ce^{+3}/Ce	δ^a (CeO_δ)	$T_{50\%}$ (°C)
4EG-Ce500	1.93	4.29	1.45	0.66	0.26	1.87	184
Ny500	2.52	3.51	1.01	0.36	0.26	1.87	267
OxEG-Ce500	2.56	3.78	1.31	0.46	0.27	1.86	308
NySint	1.25	3.13	1.03	0.31	0.25	1.88	–

[a] $\delta = 3/2\ [Ce^{+3}] + 2\ [Ce^{+4}]$

Table 3 Temperature and H_2 consumption per mole of CeO_2 obtained by TPR

Sample	1st peak		2nd peak		3rd peak		$\left(\frac{n_{H_2}}{n_{CeO_2}}\right)_{Total}$
	T (°C)	$\frac{n_{H_2}}{n_{CeO_2}}$	T (°C)	$\frac{n_{H_2}}{n_{CeO_2}}$	T (°C)	$\frac{n_{H_2}}{n_{CeO_2}}$	
4EG-Ce500	300	0.042	473	0.092	719	0.117	0.250
Ny500	388	0.011	470	0.064	712	0.114	0.189
OxEG-Ce500	393	0.015	474	0.047	728	0.100	0.162
NySint	–	–	493	0.010	736	0.079	0.089
CeO_2 std.	424	0.014	499	0.052	732	0.093	0.158

cobalt oxide to improve the O_2 selectivity towards CO_2 [11, 27, 28].

At this point, it is necessary to clarify that the new procedure with H_2O_2 could be further improved. However, in order to ensure a reliable conclusion about the effect of the method of synthesis on the COPrOx, the same synthesis conditions must be followed with the previously reported method.

Co_3O_4–CeO_2 nanoparticles: characterization and catalytic activity

Ny500 and OxEG-Ce500 samples were impregnated with three different amounts of $Co(NO_3)_2$: 0.1, 0.3, and 0.5 [molar ratio Co/(Co + Ce)], in order to observe the effect of Co loading in the COPrOx reaction for this kind of catalysts. Figure 7 shows that, as expected, the impregnation with cobalt significantly improved the conversion of CO. In the same figure, it can also be observed that methane formation starts at about 200 °C. The lowest Co loading (0.1) showed the lowest CH_4 production, and also a lower capability to eliminate the CO than the catalysts with higher cobalt loadings. From 175 °C, no significant difference was observed between the catalysts with 0.3 and 0.5 molar ratio of cobalt; however, the latter produced a smaller amount of CH_4. Konsolakis et al. [29] observed that impregnated Co_3O_4/CeO_2 catalysts with a 0.35 atomic ratio (20 wt%) showed a higher oxidative capacity than the samples with a 0.48 atomic ratio of cobalt (30 wt%). Therefore, our samples with a lower Co ratio (0.3) could be producing a higher amount of CO_2 which is fully converted to CH_4 from 200 °C, whereas the 0.5-Co/CeO_2 samples could be creating a dynamic equilibrium between CO oxidation and CO_2 methanation due to their lower oxidation capacity and higher Co loading, thus limiting the amount of CH_4. According to this, all the CeO_2 samples were impregnated with a cobalt molar ratio of 0.5 in order to see the effect of the nature of the CeO_2 used in the synthesis procedure.

Figure 8a shows that, from 200 °C, the CO conversion curves against temperature were similar for all the samples. These results showed that the surface area of the support did not influence the amount of CO converted at high temperatures. The CO conversion at 200 °C was between 88 and 94 %, with a mean selectivity towards CO_2 of 48.8 %. Methane production was observed from this temperature lowering the O_2 selectivity towards CO_2 (Fig. 8b). Woods et al. [11] reported the production of CH_4, with similar reaction conditions for a 10 wt% CoO_x/CeO_2 impregnated catalyst, but starting at a higher temperature (ca. 275 °C) than that obtained with our catalyst (225 °C). They reported that all the CO is consumed in the methanation reaction above 275 °C. Figure 8 shows that from 225 °C, CO oxidation and methanation occur simultaneously, except for 0.5-Co/NySint, in which CH_4 production raised up to ca. 99 %. The other samples showed an average production of methane of 90.0 %. This difference explained the lowest selectivity to CO_2 presented by the 0.5-Co/NySint sample. The loss of H_2—which is the valuable product being purified—due to CH_4 production is the main disadvantage of methanation; however, regardless of the catalyst used, it was never superior to 5 %.

During the catalytic experiments, below 200 °C and above 300 °C, the steady state was quickly reached at each temperature, after which the samples were taken for the chromatographic analysis. However, at 225 and 250 °C, the steady-state condition took more time to accomplish, i.e., if temperature was maintained at 225 °C, CH_4 started to be progressively formed, and the steady state was reached after 1 h (see supplementary information: 3.2.1).

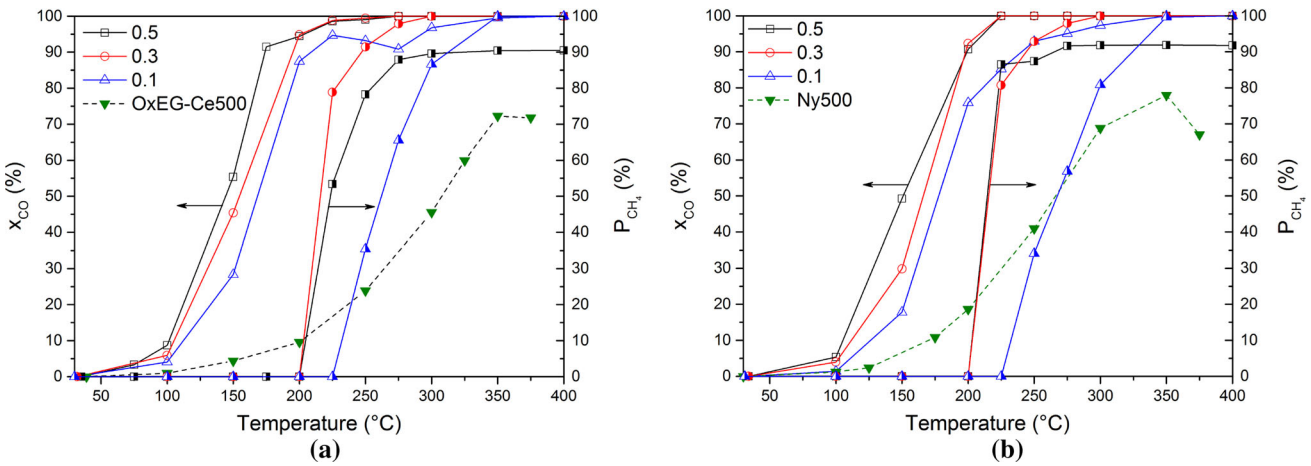

Fig. 7 Effect of Co loading on impregnated ceria. **a** OxEG-Ce500 and **b** Ny500. *Hollow symbols* CO conversion. *Half-filled symbols* methane production

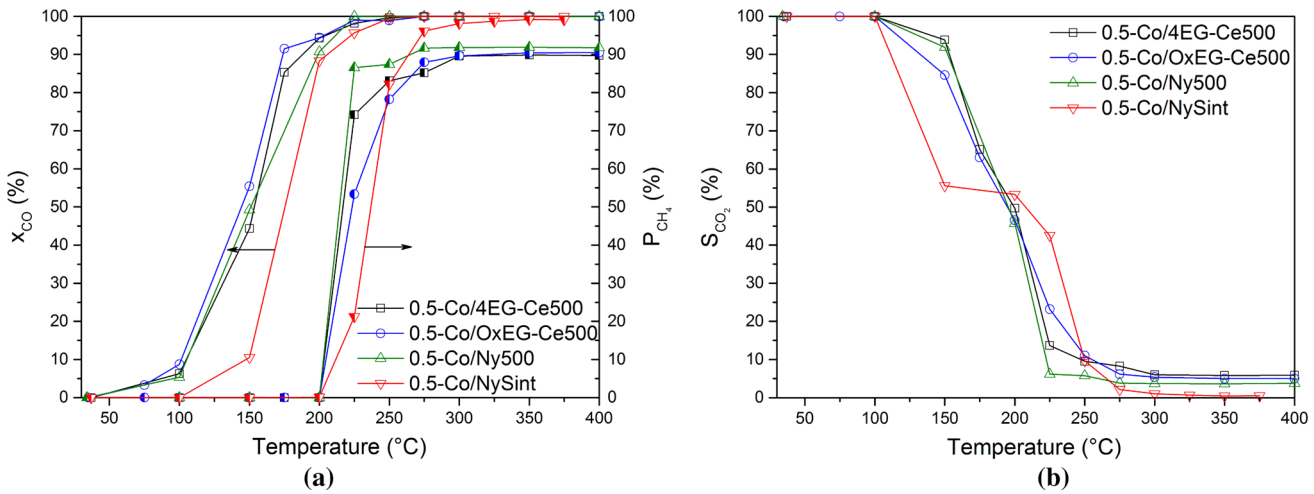

Fig. 8 COPrOx performance of catalysts of CeO_2 impregnated with a molar ratio of Co = 0.5. **a** CO conversion and **b** O_2 selectivity to CO_2. *Hollow symbols* CO conversion. *Half-filled symbols* methane production

The occurrence of this transient state could indicate that most of either metallic cobalt or CoO was gradually formed, thus increasing the methane formation rate. When temperature was increased to 300 °C, the steady state was reached immediately. This behavior was attributed to the progressive reduction of Co_3O_4 into species which are known producers of CH_4 [30, 31]. In order to gain further insight into this phenomenon, the same samples were reoxidized and analyzed by TPR (Fig. 9). The profiles obtained showed that the reduction of Co_3O_4 started at temperatures near 200 °C for all the samples. Naturally, CeO_2 nanoparticles oxidized as well within this temperature range, based on the results exposed in Fig. 6, but their reduction signals are hidden by those of Co_3O_4. However, the reduction peak of bulk CeO_2 could be observed (inset graph of Fig. 9). At the end of the catalytic test (400 °C), almost all the Co_3O_4 was converted to Co^0 through a two-step mechanism [32–34], which could be observed from the two peaks on the TPR profiles. This could explain the production of CH_4 in all samples; however, it does not elucidate why they showed a similar behavior despite their BET surface area.

The first approach to explain the behavior described above was to analyze the crystallite size. XRD measurements of the used catalysts showed the presence of Co_3O_4 in all samples, except the sintered one, which also presented some hexagonal Co^0 phase (Fig. 10). Therefore, once used, catalysts calcined at 500 °C reoxidized naturally with atmospheric O_2 showing a good regeneration capability. Crystallite size calculated for the CeO_2 phase from the XRD patterns showed almost no variation with respect to the bare CeO_2 samples. On the other hand, the same parameter calculated with the Co_3O_4 peaks (and Co^0 for 0.5-Co/NySint) showed high values indicating a probable size effect on the mechanism of CH_4 formation. TEM/STEM analysis allowed a greater insight into this issue.

Figure 11 shows TEM images obtained for the synthesized powder samples suspended in isopropanol. The comparison with Fig. 2 and the nature of the synthesis procedure allowed us to claim that the large crystals observed are Co_3O_4 with small CeO_2 nanoparticles over or inside them. This fact was confirmed by STEM analysis (see supplementary information: 3.2.2). Therefore, the impregnation of the CeO_2 nanoparticles with the cobalt nitrate solution and subsequent drying and calcination would form large particles of Co_3O_4 containing several CeO_2 nanoparticles distributed over the surface or inside them. This arrangement would also explain the decrease on the BET surface area shown by the bimetallic samples (Table 4). The higher exposed area of these large crystals of Co_3O_4 contributed to the formation of CH_4 in similar amounts despite the CeO_2 used. According to this, the CO could be adsorbed and oxidized by the cobalt surface and, at the same time, the ceria would regenerate the oxygen vacancies formed on it. The former claim was confirmed by performing an additional reaction test, feeding only CO and hydrogen (in He) into the reactor for the 0.5-Co/Ny500 sample (see supplementary information: 3.2.3). CH_4 formation through CO (without O_2) was achieved at 250 °C, whereas in the presence of O_2 it started just above 200 °C, showing that methanation preferentially occurs through CO_2 between 200 and 250 °C, and with CO above this latter temperature. The second claim became clear on the higher final CH_4 production presented on 0.5-Co/NySint: the lowest surface area of CeO_2 did not allow an efficient reoxidation, which has been confirmed by the presence of Co^0 in the XRD measurements performed after reaction (Fig. 10). In fact, Konishcheva et al. [35]

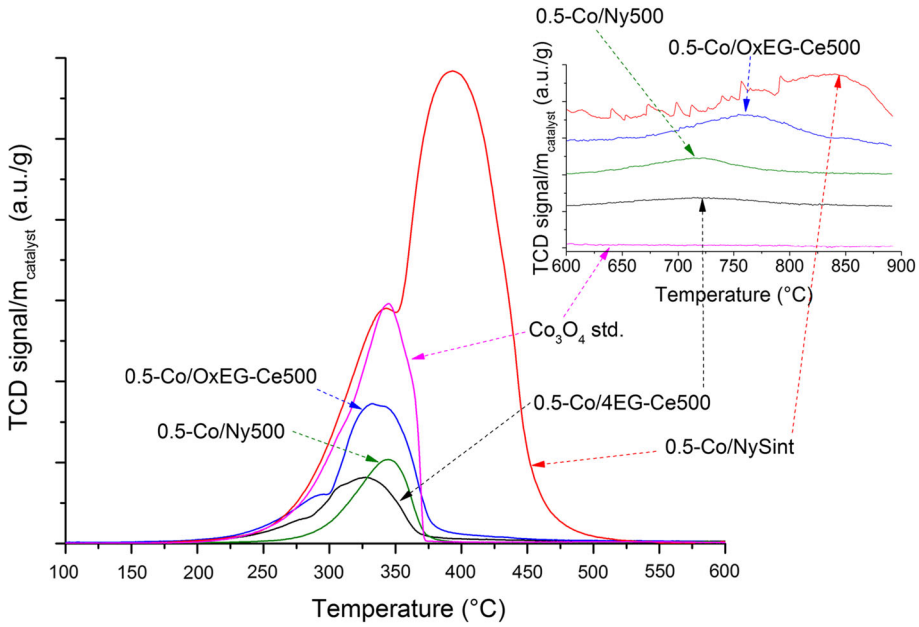

Fig. 9 TPR profiles of the reoxidized CoO_x/CeO_2 catalysts

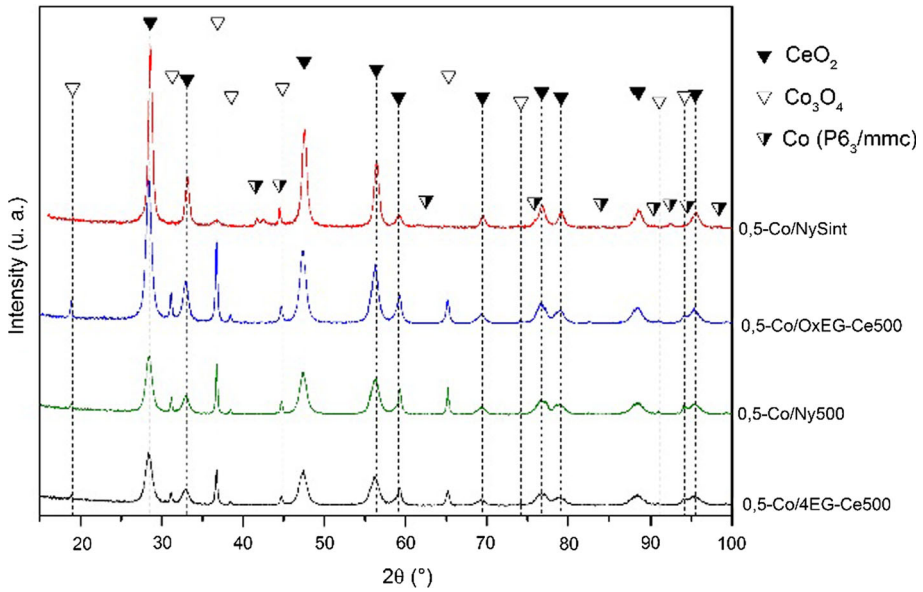

Fig. 10 XRD patterns of CoO_x/CeO_2 impregnated catalysts

synthesized a Co/CeO_2 catalyst by incipient wetness impregnation—among others—to selectively convert CO into CH_4 through the inhibition of CO_2 methanation, in a H_2-rich gas mixture composed by CO, CO_2, and H_2O (He balance). This dynamic reoxidation process seemed to be the key in this kind of catalyst. Therefore, the stability of the sample 0.5-Co/OxEG-Ce500 was evaluated at 200 °C for 115.7 h (supplementary information, Fig. S.4), and the conversion of CO and the selectivity to CO_2 were similar to the reported values (Fig. 8): 91.4 ± 0.005 and 56.0 ± 0.009 %, with a slight decrease in the former.

In brief, the BET surface area of the support would be less important than the intimate contact between CeO_2 and Co_3O_4. The higher the interaction, the slower the rate of reduction and the more stable the catalyst would be [36]. Yan et al. [37], for example, synthesized a mesoporous Co–Ce oxide, with an optimal cobalt molar ratio Co/(Co + Ce) = 0.48 (30 wt%) and obtained CO conversions of 100 % at 200 °C, but without methane production. This shows that the high interaction is the key for this kind of mixed catalyst. These authors found a maximum Co loading of 30 wt%, from which CO conversion starts to decrease. Even though they did not report results at temperatures higher than 220 °C, a conversion window obtained was 70 °C, whereas our catalysts—with a similar Co loading—presented a conversion window of 200 °C,

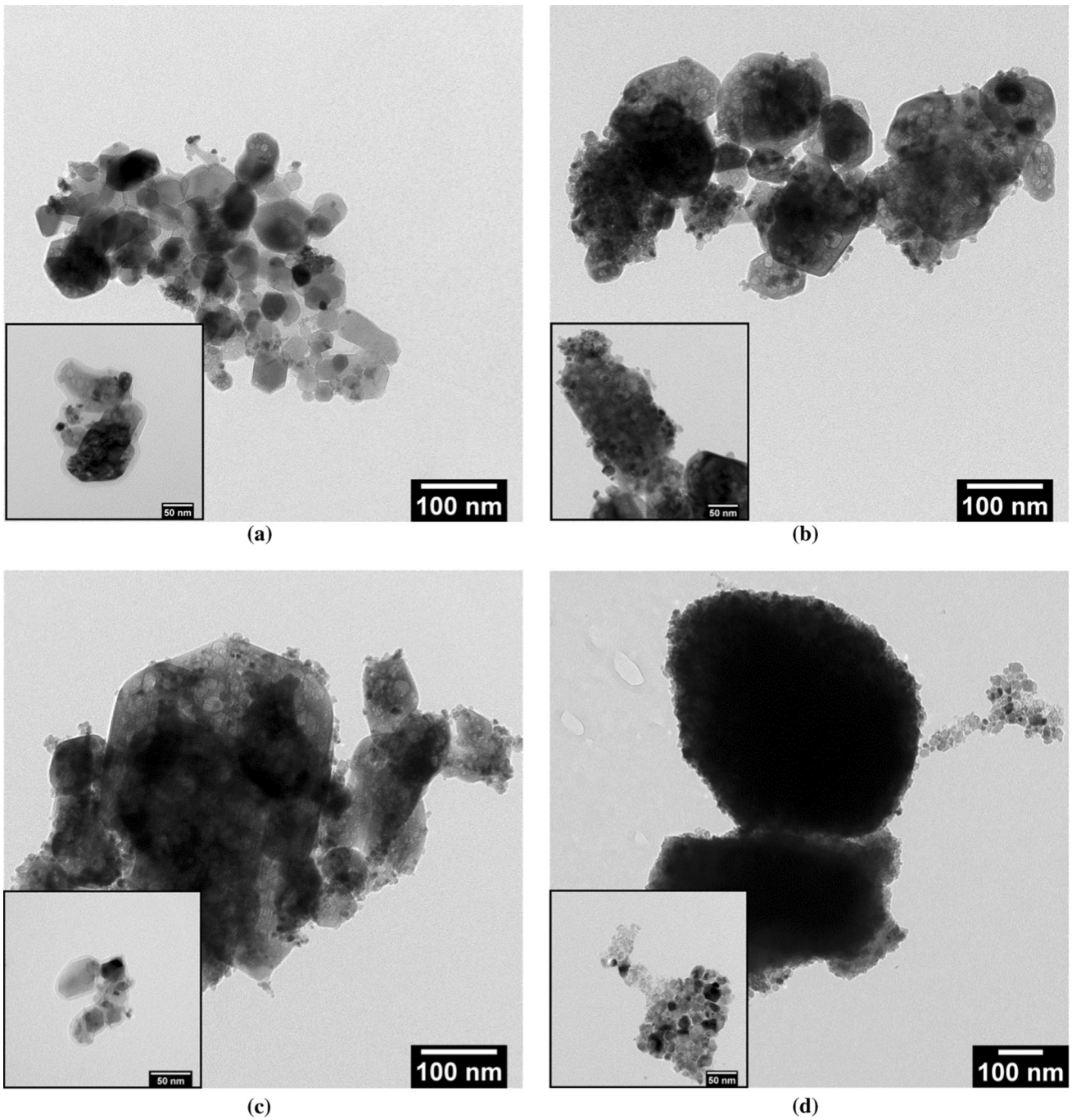

Fig. 11 TEM images of the 0.5-CoO_x/CeO_2 samples. **a** 0.5-Co/4EG-Ce500, **b** 0.5-Co/Ox-Ce500, **c** 0.5-Co/Ny500, and **d** 0.5-Co/NySint

but at higher temperatures. On the other hand, preliminary results of a CoO_x–CeO_2 catalyst synthesized by a solvothermal method with a CeO_2 of high area (111.6 m^2/g) showed similar CO conversion values to the samples impregnated with Co/(Co + Ce) = 0.1 (Fig. 7), but with less amount of cobalt (see supplementary information: 3.2.5). Therefore, the dynamic reoxidation promoted by the higher area of the CeO_2 could be more important than the amount of cobalt. This behavior makes our impregnated 0.5-Co/CeO_2 catalysts suitable candidates for the treatment of the exhaust gases from the first step of the water gas shift reactor (WGSR): the high-temperature shift (HTS) where the exhaust reaches temperatures from 310 to 450 °C [38], avoiding the need for the low-temperature WGS reactor with an H_2 maximum loss of 5 %. Although a more complete analysis with CO_2 and H_2O should be performed,

Table 4 Crystallite size and BET surface area of bimetallic catalysts

Sample	Crystallite size (nm)		BET (m^2/g)
	D_{Ce}	D_{Co}	
0.5-Co/4EG-Ce500	9.8 ± 0.7	44.3 ± 9.5	40.8
0.5-Co/OxEG-Ce500	12.6 ± 1.0	50.1 ± 6.1	28.7
0.5-Co/Nyacol	10.2 ± 1.1	66.5 ± 13.7	31.6
0.5-Co/NySint[a]	17.5 ± 3.1	16.8 (Co_3O_4)	5.1
		70.2 (Co)	

[a] The D_{Co} for this sample was calculated using just one peak for each cobalt species, due to the weakness of their signal

we believe that these results could provide a better insight into the mechanism of CO elimination at high temperatures and into the oxidation-regeneration mechanism between Co and Ce.

Conclusions

CeO_2 nanoparticles of similar sizes and surface areas have a different activity in the COPrOx reaction depending on the synthesis method employed. The CeO_2 that exhibited the lowest temperature at the 50 % CO conversion, for similar BET surface areas, presented the highest surface O/Ce ratio (XPS). Carbonates measured by FTIR after synthesis showed a strong influence on the reactivity of the ceria, i.e., lower amounts implied higher CO conversion values.

The addition of H_2O_2 to the synthesis procedure highly improved the CeO_2 nanoparticle yield, but also increased the amount of carbonate adsorbed species due to the reaction between EG and H_2O_2, lowering the CO conversion as a result.

Impregnation with three different amounts of $Co(NO_3)_2$ (0.1, 0.3, and 0.5 Co molar ratio) showed that CO elimination improved significantly with respect to bare CeO_2 according to literature. A molar ratio of 0.5 showed the higher CO conversion with the lower CH_4 production. The comparison of CoO_x/CeO_2 catalysts with 0.5 of cobalt synthesized with CeO_2 obtained in four different ways, and presenting four different profiles in the COPrOx tests, showed that the specific surface area and the nature of CeO_2 do not influence the activity of the catalyst at temperatures higher than 200 °C. At this temperature, a time-dependent methanation started due to the reaction between CO_2 and H_2. However, above 250 °C, the reaction between CO and H_2 became important, thus contributing to CO elimination with a small H_2 loss (<5 %). As a result of this behavior, CO can be totally eliminated in a wide temperature range. The reduction of Co_3O_4 into CoO and/or metallic Co could be responsible for CH_4 production, and their larger size with respect to ceria nanoparticles could be the cause of the independence in the removal of CO with the specific BET surface area. The wet impregnation method provided a Co_3O_4/CeO_2 catalyst for the complete CO elimination with a wide conversion window (200 °C), a slight H_2 loss, and suitable for the direct treatment of exhaust gases from HTS of the WGS reactor.

Acknowledgements The authors wish to acknowledge the financial support received from UNL, ANPCyT, and CONICET. Thanks are given to María Fernanda Mori for the XPS measurements and to Esther María Fixman for the BET measurements and her advice on the technique.

References

1. Adams FC, Barbante C (2013) Nanoscience, nanotechnology and spectrometry. Spectrochim Acta Part B 86:3–13. doi:10.1016/j.sab.2013.04.008
2. Mangematin V, Walsh S (2012) The future of nanotechnologies. Technovation 32:157–160. doi:10.1016/j.technovation.2012.01.003
3. Bion N, Epron F, Moreno M, Mariño F, Duprez D (2008) Preferential oxidation of carbon monoxide in the presence of hydrogen (PROX) over noble metals and transition metal oxides: advantages and drawbacks. Top Catal 51:76–88. doi:10.1007/s11244-008-9116-x
4. Wootsch A (2004) Preferential oxidation of carbon monoxide in the presence of hydrogen (PROX) over ceria-zirconia and alumina-supported Pt catalysts. J Catal 225:259–266. doi:10.1016/j.jcat.2004.04.017
5. Xu G, Chen X, Zhang Z-G (2006) Temperature-staged methanation: an alternative method to purify hydrogen-rich fuel gas for PEFC. Chem Eng J 121:97–107. doi:10.1016/j.cej.2006.05.010
6. Xu G, Zhang Z-G (2006) Preferential CO oxidation on Ru/Al_2O_3 catalyst: an investigation by considering the simultaneously involved methanation. J Power Sources 157:64–77. doi:10.1016/j.jpowsour.2005.07.028
7. Lawrence NJ, Brewer JR, Wang L et al (2011) Defect engineering in cubic cerium oxide nanostructures for catalytic oxidation. Nano Lett 11:2666–2671. doi:10.1021/nl200722z
8. Peiretti LF, Tiscornia IS, Miró EE (2013) Study of the synthesis of CeO_2 nanoparticles for their use in CO preferential oxidation (COPrOx). Chem Eng J 223:507–515. doi:10.1016/j.cej.2013.02.121
9. Gómez LE, Tiscornia IS, Boix AV, Miró EE (2012) CO preferential oxidation on cordierite monoliths coated with Co/CeO_2 catalysts. Int J Hydrog Energy 37:14812–14819. doi:10.1016/j.ijhydene.2012.01.159
10. Gómez-Cuaspud JA, Schmal M (2013) Nanostructured metal oxides obtained by means polymerization-combustion at low temperature for CO selective oxidation. Int J Hydrog Energy 38:7458–7468. doi:10.1016/j.ijhydene.2013.04.024
11. Woods MP, Gawade P, Tan B, Ozkan US (2010) Preferential oxidation of carbon monoxide on Co/CeO_2 nanoparticles. Appl Catal B 97:28–35. doi:10.1016/j.apcatb.2010.03.015
12. Konysheva EY, Francis SM (2013) Identification of surface composition and chemical states in composites comprised of phases with fluorite and perovskite structures by X-ray photoelectron spectroscopy. Appl Surf Sci 268:278–287. doi:10.1016/j.apsusc.2012.12.079

13. Fang J, Bi X, Si D, Jiang Z, Huang W (2007) Spectroscopic studies of interfacial structures of CeO_2–TiO_2 mixed oxides. Appl Surf Sci 253:8952–8961. doi:10.1016/j.apsusc.2007.05.013
14. Poggio E, Jobbágy M, Moreno M, Laborde M, Mariño F, Baronetti G (2011) Influence of the calcination temperature on the structure and reducibility of nanoceria obtained from crystalline $Ce(OH)CO_3$ precursor. Int J Hydrog Energy 36:15899–15905. doi:10.1016/j.ijhydene.2011.09.026
15. Bourja L, Bakiz B, Benlhachemi A et al (2012) Structural modifications of nanostructured ceria CeO_2, xH_2O during dehydration process. Powder Technol 215–216:66–71. doi:10.1016/j.powtec.2011.09.008
16. Rios E, Nguyen-Cong H, Marco JF, Gancedo JR, Chartier P, Gautier JL (2000) Indirect oxidation of ethylene glycol by peroxide ions at $Ni_{0.3}Co_{2.7}O_4$ spinel oxide thin film electrodes. Electrochim Acta 45:4431–4440. doi:10.1016/S0013-4686(00)00498-9
17. Trovarelli A (1996) Catalytic properties of ceria and CeO_2-containing materials. Catal Rev 38:439–520. doi:10.1080/01614949608006464
18. Larachi F, Pierre J, Adnot A, Bernis A (2002) Ce 3d XPS study of composite $CexMn_{1-x}O_{2-y}$ wet oxidation catalysts. Appl Surf Sci 195:236–250. doi:10.1016/s0169-4332(02)00559-7
19. Rebellato J, Natile MM, Glisenti A (2008) Influence of the synthesis procedure on the properties and reactivity of nanostructured ceria powders. Appl Catal A 339:108–120. doi:10.1016/j.apcata.2007.12.031
20. Biesinger MC, Payne BP, Grosvenor AP, Lau LWM, Gerson AR, Smart RSC (2011) Resolving surface chemical states in XPS analysis of first row transition metals, oxides and hydroxides: Cr, Mn, Fe, Co and Ni. Appl Surf Sci 257:2717–2730. doi:10.1016/j.apsusc.2010.10.051
21. Chuang TJ, Brundle CR, Rice DW (1976) Interpretation of the X-ray photoemission spectra of cobalt oxides and cobalt oxide surfaces. Surf Sci 59:413–429. doi:10.1016/0039-6028(76)90026-1
22. Stoch J, Gablankowska-Kukucz J (1991) The effect of carbonate contaminations on the XPS O 1 s band structure in metal oxides. Surf Interface Anal 17:165–167. doi:10.1002/sia.740170308
23. Damyanova S, Perez CA, Schmal M, Bueno JMC (2002) Characterization of ceria-coated alumina carrier. Appl Catal A 234:271–282. doi:10.1016/s0926-860x(02)00233-8
24. Katta L, Sudarsanam P, Thrimurthulu G, Reddy BM (2010) Doped nanosized ceria solid solutions for low temperature soot oxidation: zirconium versus lanthanum promoters. Appl Catal B 101:101–108. doi:10.1016/j.apcatb.2010.09.012
25. Marrero-Jerez J, Larrondo S, Rodríguez-Castellón E, Núñez P (2014) TPR, XRD and XPS characterisation of ceria-based materials synthesized by freeze-drying precursor method. Ceram Int 40:6807–6814. doi:10.1016/j.ceramint.2013.11.143
26. Deeprasertkul C, Longloilert R, Chaisuwan T, Wongkasemjit S (2014) Impressive low reduction temperature of synthesized mesoporous ceria via nanocasting. Mater Lett 130:218–222. doi:10.1016/j.matlet.2014.05.124
27. Razeghi A, Khodadadi A, Ziaei-Azad H, Mortazavi Y (2010) Activity enhancement of Cu-doped ceria by reductive regeneration of CuO–CeO_2 catalyst for preferential oxidation of CO in H_2-rich streams. Chem Eng J 164:214–220. doi:10.1016/j.cej.2010.07.064
28. Chen Y, Liu D, Yang L et al (2013) Ternary composite oxide catalysts CuO/Co_3O_4–CeO_2 with wide temperature-window for the preferential oxidation of CO in H_2-rich stream. Chem Eng J 234:88–98. doi:10.1016/j.cej.2013.08.063
29. Konsolakis M, Sgourakis M, Carabineiro SAC (2015) Surface and redox properties of cobalt-ceria binary oxides: on the effect of Co content and pretreatment conditions. Appl Surf Sci. doi:10.1016/j.apsusc.2015.02.188
30. Ko E-Y, Park ED, Seo KW, Lee HC, Lee D, Kim S (2006) A comparative study of catalysts for the preferential CO oxidation in excess hydrogen. Catal Today 116:377–383. doi:10.1016/j.cattod.2006.05.072
31. Marbán G, López I, Valdés-Solís T, Fuertes AB (2008) Highly active structured catalyst made up of mesoporous Co_3O_4 nanowires supported on a metal wire mesh for the preferential oxidation of CO. Int J Hydrog Energy 33:6687–6695. doi:10.1016/j.ijhydene.2008.07.067
32. Lin H-K, Chiu H-C, Tsai H-C, Chien S-H, Wang C-B (2003) Synthesis, characterization and catalytic oxidation of carbon monoxide over cobalt oxide. Catal Lett 88:169–174. doi:10.1023/A:1024013822986
33. Liotta LF, Di Carlo G, Pantaleo G, Venezia AM, Deganello G (2006) Co_3O_4/CeO_2 composite oxides for methane emissions abatement: relationship between Co_3O_4–CeO_2 interaction and catalytic activity. Appl Catal B 66:217–227. doi:10.1016/j.apcatb.2006.03.018
34. Tang C-W, Kuo M-C, Lin C-J, Wang C-B, Chien S-H (2008) Evaluation of carbon monoxide oxidation over CeO_2/Co_3O_4 catalysts: effect of ceria loading. Catal Today 131:520–525. doi:10.1016/j.cattod.2007.10.026
35. Konishcheva MV, Potemkin DI, Snytnikov PV et al (2015) Selective CO methanation in H2-rich stream over Ni-, Co- and Fe/CeO2: effect of metal and precursor nature. Int J Hydrog Energy 40:14058–14063. doi:10.1016/j.ijhydene.2015.07.071
36. Wang H, Miller JT, Shakouri M et al (2013) XANES and EXAFS studies on metal nanoparticle growth and bimetallic interaction of Ni-based catalysts for CO_2 reforming of CH_4. Catal Today 207:3–12. doi:10.1016/j.cattod.2012.09.015
37. Yan C-F, Chen H, Hu R-R et al (2014) Synthesis of mesoporous Co–Ce oxides catalysts by glycine-nitrate combustion approach for CO preferential oxidation reaction in excess H2. Int J Hydrog Energy 39:18695–18701. doi:10.1016/j.ijhydene.2014.01.024
38. Reddy GK, Smirniotis PG (2015) High-temperature WGS reaction. In: Reddy GK, Smirniotis PG (eds) Water Gas Shift Reaction, vol 2. Elsevier, Amsterdam, pp 21–45